Geophysical Research Letters

Supporting Information for

Controls on Ice Cliff Formation, Distribution and Characteristics on Debris-Covered Glaciers

M. Kneib[1, 2], Catriona Fyffe[3], Evan S. Miles[1], Shayna Lindemann[1], Thomas E. Shaw[1], Pascal Buri[1], Michael McCarthy[1], Boris Ouvry[4], Andreas Vieli[4], Yota Sato[5], Philip D.A Kraaijenbrink[6], Chuanxi Zhao[7,8], Peter Molnar[2], Francesca Pellicciotti[1,3]

[1] High Mountain Glaciers and Hydrology Group, Swiss Federal Institute, WSL, Birmensdorf, Switzerland.

[2] Institute of Environmental Engineering, ETH Zürich, Zürich, Switzerland

[3] Department of Geography and Environmental Sciences, Northumbria University, Newcastle upon Tyne, UK

[4] Department of Geography, University of Zurich, 8057 Zurich, Switzerland

[5] Graduate School of Environmental Studies, Nagoya University, Nagoya, Japan

[6] Utrecht University, Department of Physical Geography, PO Box 80115, 3508 TC, Utrecht, The Netherlands.

[7] College of Earth and Environmental Sciences, Lanzhou University, Lanzhou 730000, China

[8] State Key Laboratory of Tibetan Plateau Earth System, Environment and Resources (TPESER), Institute of Tibetan Plateau Research, Chinese Academy of Sciences

Contents of this file

Text S1. Ice cliff formation

1.1. Multi-temporal UAV data

Here we took advantage of multi-temporal Unsupervised Aerial Vehicle (UAV) surveys over portions of five of the studied glaciers: Trakarding, Langtang, Lirung, 23K and 24K Glaciers (Brun et al., 2016; Chuanxi et al., in prep; Immerzeel et al., 2014; Kraaijenbrink et al., in prep; Sato et al., 2021; Table S1; Fig. S1). The surveys were conducted over a period of 2-5 years, with a repeat time of at least one year (Table S1). The resolution of the original DEMs and orthoimages varied between 0.1 and 0.2 m, and they were all co-registered using surrounding stable terrain (see details in Chuanxi et al., in prep.; Kraaijenbrink et al., in prep.; Sato et al., 2021;). From 2016 we used all available cloudless Sentinel-2 images (10m resolution) of the survey domains taken during the melt season to identify seasonal ponds. These images were atmospherically-corrected using the MAJA processing workflow (Hagolle et al., 2015).

1.2. Identification of newly-formed ice cliffs

We manually identified newly-formed cliffs in the orthoimages as patches of bare ice that were not visible in previous images, irrespective of their slope, accounting for glacier flow (Kneib et al., 2021). The outlines of these newly-formed cliffs were further derived manually. The DEMs were resampled to 1m to derive slope and aspect of all pixels, and to map supraglacial channels using a flow-routing algorithm following the same approach as for the Pléiades DEMs (Schwangart & Scherler, 2014).

The mechanisms underlying the ice cliff formation were determined by a single operator based on 1/ the proximity to ponds (including seasonal ponds identified in the Sentinel-2 images), visible streams or supraglacial channels and 2/ the initial shape of the cliffs and the general organisation of the glacier surface at this location. This classification, as well as the ice cliff outlines, were then validated by a second independent operator.

1.3. Main results

We identified 202 newly-formed cliffs (38 for Langtang, 27 for Lirung, 57 for Trakarding, 38 for 23K and 42 for 24K) and classified the formation mechanisms as 'pond-influenced', 'stream-influenced', 'crevasses' or 'undefined' when the formation mechanism was not clear. Since the same classification was used for newly-formed cliffs and the entire cliff population, we could directly compare the characteristics of the newly-formed cliff pixels with the values obtained

from looking at the entire cliff population with the Pléiades data, specifically for the UAV survey domains (Fig. S2-S5).

The proportion of cliff categories was mostly consistent between newly-formed cliffs and the entire cliff population, except for Lirung where the triggering mechanism for most newly-formed cliffs could not be determined, and for Trakarding, where the proportion of pond-influenced new cliffs was greater (Fig. S2). There were no consistent differences in the slope distribution of the newly-formed cliffs and the whole cliff population within these five domains. The slope of crevasses was consistently shallower, which was likely due to the DEM resolution being too coarse to represent their slope accurately.The slope distribution of the stream-influenced, pond-influenced and undefined cliffs was overall similar for the total cliff population, while the slope of the newly-formed pond-influenced cliffs tended to be steeper than for the other categories (Fig. S3). The most striking differences were visible in the aspect distributions, where the full cliff population was generally oriented north-west to north, except for Lirung, while the newly-formed cliffs seemed to either be completely random (e.g. for Trakarding) or preferentially oriented in the general glacier flow direction (Fig. S4). In terms of cliff size, the newly-formed cliffs were consistently smaller, and so for all categories (Fig. S5).

1.4. Discussion points

This focused study of the characteristics of newly-formed cliffs enabled us to link ice cliff formation with ice cliff distribution. Ice cliff formation mechanisms are indeed expected to have a strong influence on the distribution of ice cliffs across the glacier surface due to the high cliff birth and death rates (Kneib et al., 2021). The relatively long-term monitoring periods and the large number of sites covered here, with various glaciological and climatic characteristics (Fugger et al., 2022; Kneib et al., 2022; Sato et al., 2021), enabled us to identify a large number of ice cliff formation events and outline a number of interesting patterns. The main outcome was that as for ice cliff distribution, the formation mechanisms were driven by the glacier hydrology, including the proglacial or englacial hydrology for some of the crevasse-opening scenarios (Fig. S6). Other interesting findings were that there was no preferential north-facing aspect for newly-formed cliffs, which was additional evidence for the faster reburial of south-facing cliffs (Buri & Pellicciotti, 2018). Additionally, newly-formed cliffs tended to be smaller in size, which confirmed the observations made at other sites with coarser resolution sensors (Kneib et al., 2021).

There remained limitations in the analysis of these patterns due to the relatively small area covered and the observational bias to the lower part of the debris-covered area of these glaciers. Additionally, despite the relatively high frequency of repeat surveys, the time intervals usually remained too long to precisely describe the formation mechanisms (Kneib et al., 2022). For instance, the 'pond-influenced' formations could have been due to pond drainage or filling, but this was not always clear due to too long time intervals between images so we kept the generic term. Similarly for 'stream-influenced' formations, the exact mechanism was not always clear and the presence of water in the channel could not always be verified from the images (based on field observations from the various sites we anyway expected the water level in the streams to vary considerably seasonally), so a classification based on the presence of meanders in the surface DEMs was usually a strong argument to classify the newly-formed cliffs as stream-influenced. Crevasses were easily identifiable from their elongated, sometimes slightly curved shapes, but the triggering mechanism responsible for crevasse opening could not always be clearly identified (Reid & Brock, 2014; Steiner et al., 2019) and could vary from simple shear at the glacier lateral margins (for 24K especially) to the influence of proglacial lakes or streams

entering the glacier laterally (for Trakarding especially, Fig. S6). We did not see any evidence of englacial conduit collapse for the duration of the monitoring periods, although the development of concentric crevasses preluding some of these events on debris-covered glaciers have been described at several locations in the Swiss Alps (Mölg et al., 2019; Egli et al., 2021; Fig. S6). Similarly, we did not have enough evidence to categorize formation events as being solely caused by slope steepening from differential melt, and for the large majority of events the hydrology or the glacier dynamics seemed to play a decisive role (Sharp, 1949; Moore, 2021). These formation events were actually most likely due to a combination of factors leading to slope steepening prior to the emergence of the new cliff, and the formation mechanisms that we identified most likely mainly reflected the 'triggering' event leading to debris removal and cliff formation.

Text S2. Ice cliff, pond and stream delineation

Ice cliffs and ponds were derived automatically in each Pléiades scene following the Spectral Curvature method for cliffs, which is based solely on spectral characteristics (Kneib et al., 2020), and the Normalized Difference Water Index (NDWI) for ponds (McFeeters, 1998; Watson et al., 2016; 2018; Miles et al., 2017b). False positive identifications due to local shadows or changing geology were filtered out manually (Fig. S7, S8).

We accounted for pond seasonality by automatically mapping areas with a Normalized Difference Water Index (NDWI) value greater than 0.1 in all 10 m resolution Sentinel-2 images of the previous melt season (May-November), after filtering clouds and shaded areas (Kneib et al., 2020; McFeeters et al., 1998; Watson et al., 2018). We retained as ponds (at least temporary ones) the areas for which more than three cloudless Sentinel-2 images were available and where the NDWI was greater than 0.1 more than 33% of the time. False positives were removed manually and the resulting pond density values are consistent with the ones from the Pléiades images (Fig. S9) and additionally account for strong seasonal variability at some of the sites (E. S. Miles et al., 2017b; Watson et al., 2016). The final pond outlines were defined as the union between the Pléiades and Sentinel-2 outlines.

The minimum cliff and pond detection size is given by the resolution of the Pléiades data (2m). The uncertainties in the mapping of cliffs and ponds were assessed by eroding and dilating the mapped features by 0.5 pixels (1 m for cliffs, 5 m for ponds), and taking the upper (+42% for cliffs, +77% for ponds) and lower (-38% and -49%) area bounds as uncertainty values (Brun et al., 2018; Fig. S10). The Pléiades outlines were validated at one of the glaciers with near-contemporaneous outlines obtained from a 1m-resolution UAV orthoimage (Fig. S11).

Using the Pléiades DEMs, we mapped supraglacial channels (used as a proxy for supraglacial streams) across all the glaciers using the TopoToolbox flow routing algorithm (Schwangart & Scherler, 2014), after filling the DEM sinks shallower than 5m and removing the crevassed areas. These 'streams' were defined as the pixels with a contributing upstream area higher than 10000 m^2 and were used to calculate stream sinuosity (Anderson, Armstrong, Anderson, Scherler et al., 2021; Mölg et al., 2020).

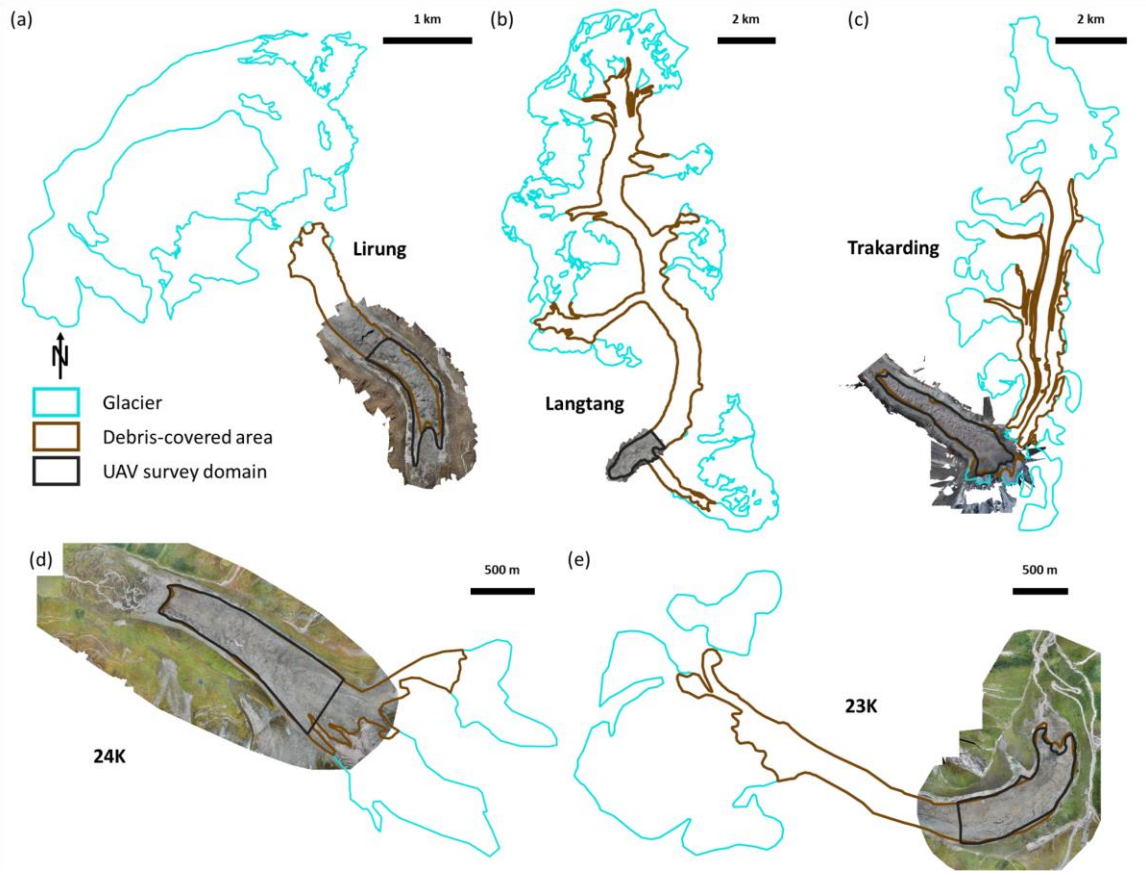

Figure S1. UAV survey domain for each glacier. Background images are the (a) Lirung 10/2017, (b) Langtang 04/2018, (c) Trakarding 10/2017, (d) 24K 09/2018 and (e) 23K 09/2018 UAV orthoimages. Glacier and debris outlines are the ones derived from the corresponding Pléiades images.

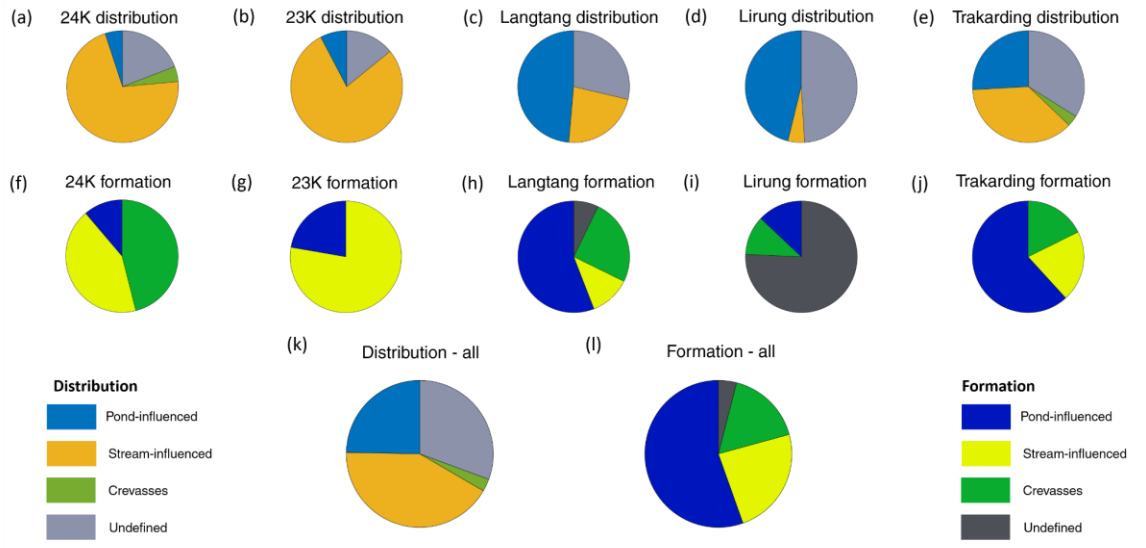

Figure S2. Area proportion of different ice cliff categories within the five UAV survey domains from the total cliff population derived from the Pléiades data (a-e) and from the newly-formed

cliffs identified in the multi-temporal UAV data (f-j). (k-l) Combination of all five sites, weighted by the area of the survey domain and the duration of the UAV study period.

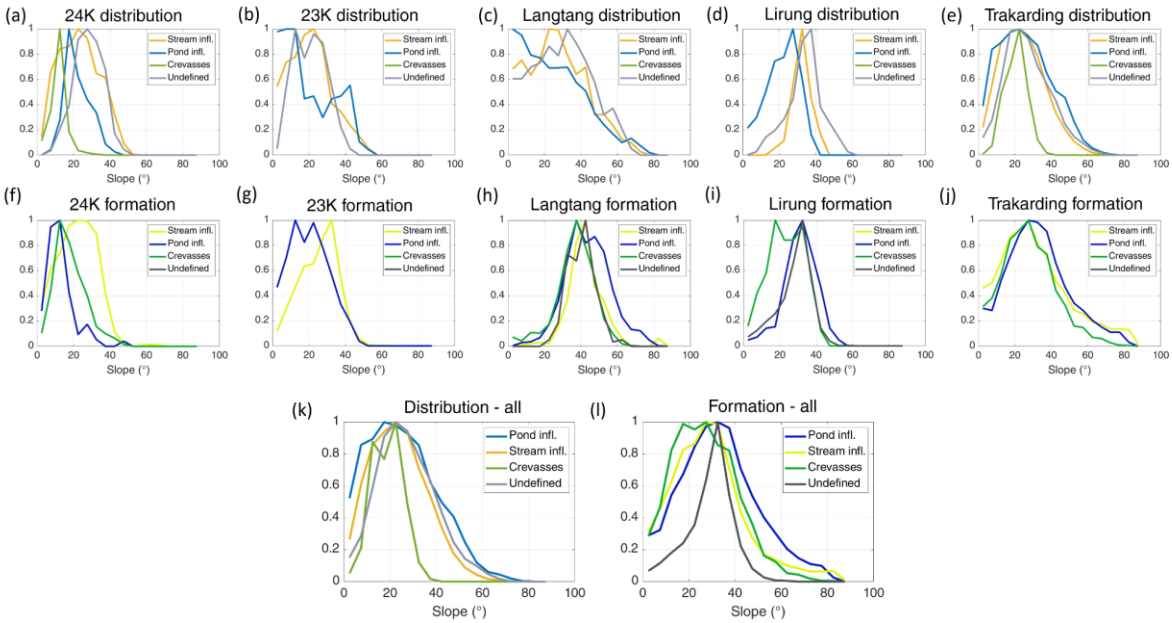

Figure S3: Slope distribution of the pixels of different ice cliff categories within the five UAV survey domains from the total cliff population derived from the Pléiades data (a-e) and from the newly-formed cliffs identified in the multi-temporal UAV data (f-j). (k-l) Combination of all five sites.

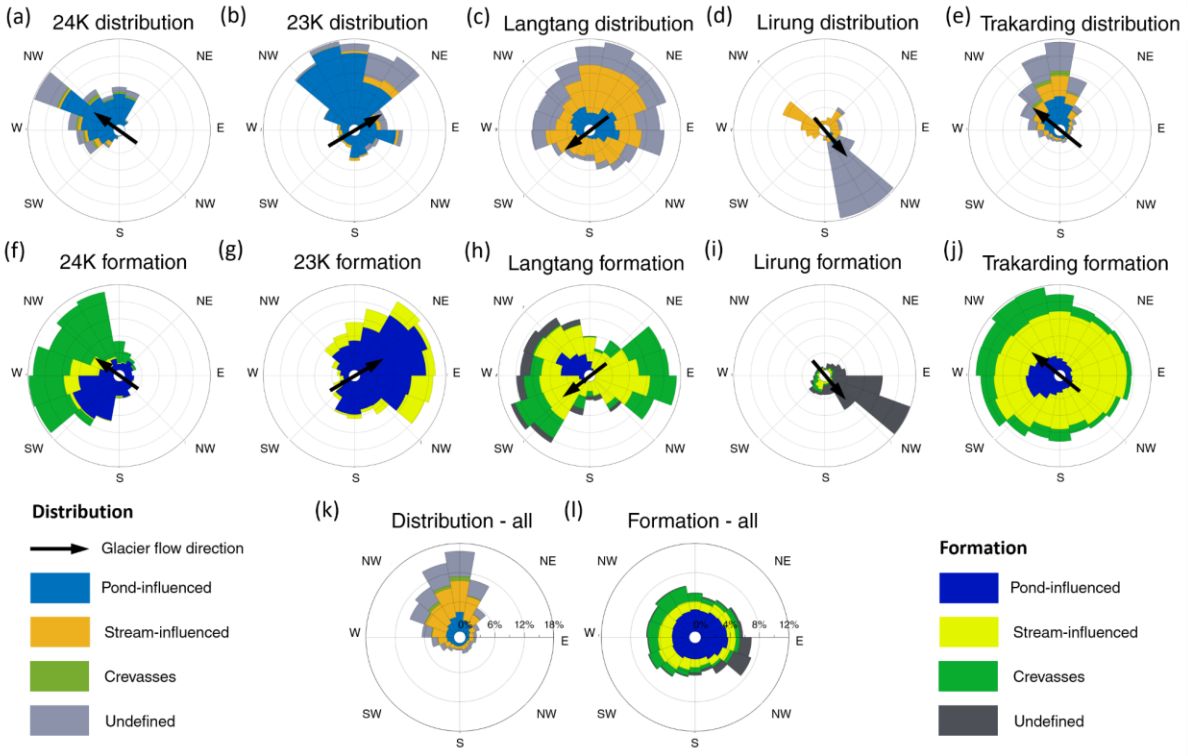

Figure S4: Aspect distribution of the pixels of different ice cliff categories within the five UAV survey domains from the total cliff population derived from the Pléiades data (a-e) and from the newly-formed cliffs identified in the multi-temporal UAV data (f-j). (k-l) Combination of all five sites.

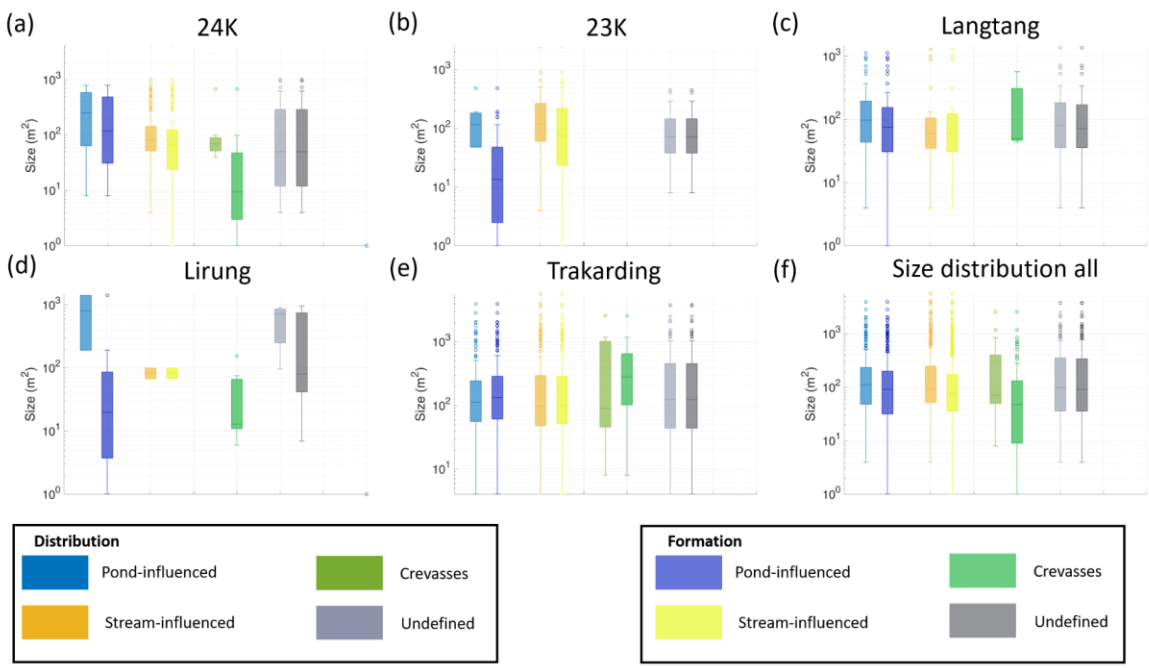

Figure S5: Size distribution of the cliffs of different ice cliff categories within the five UAV survey domains from the total cliff population derived from the Pléiades data and from the newly-formed cliffs identified in the multi-temporal UAV data (a-e). (f) Combination of all five sites.

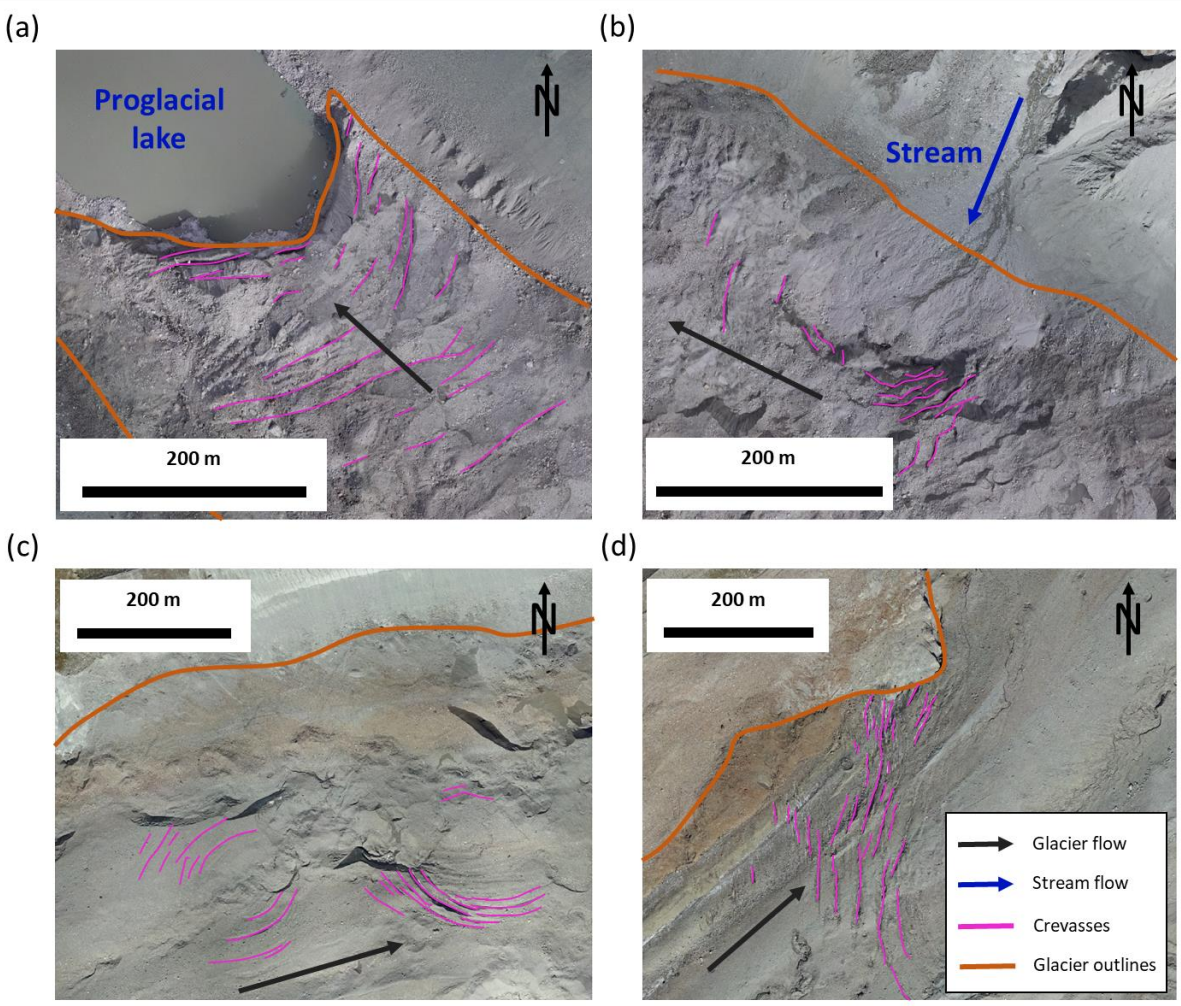

Figure S6: Crevasse patterns on (a-b) Trakarding Glacier, 10/2019 and (c-d) Zmutt Glacier, 09/2018. (a) Influence from a proglacial lake. (b) Stream entering the glacier from the side. (c) Circular crevasses symptomatic of englacial or subglacial conduit, likely preceding a conduit collapse. (d) Simple shear situation at the glacier lateral margins.

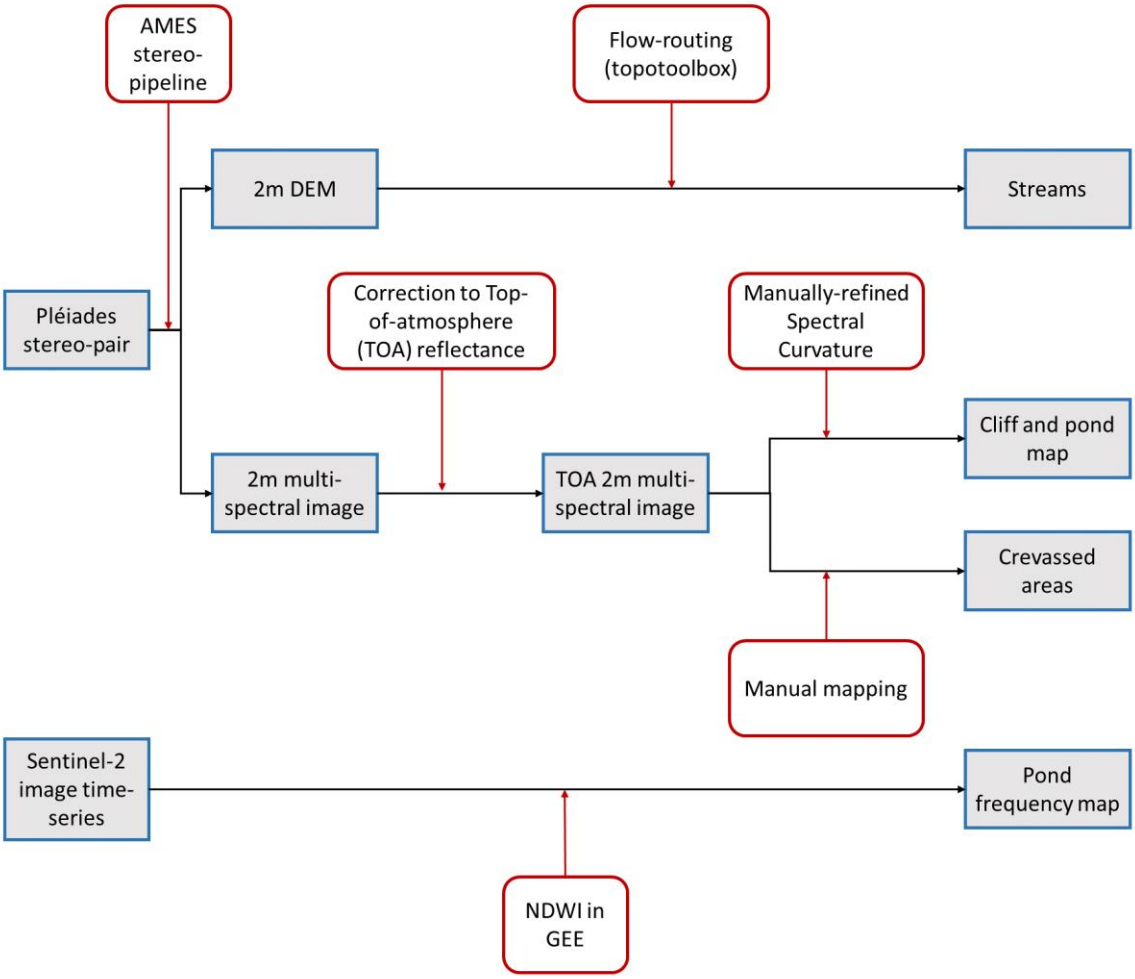

Figure S7: Processing steps of the Pléiades and Sentinel-2 images to obtain final cliff, pond, stream and crevasse maps.

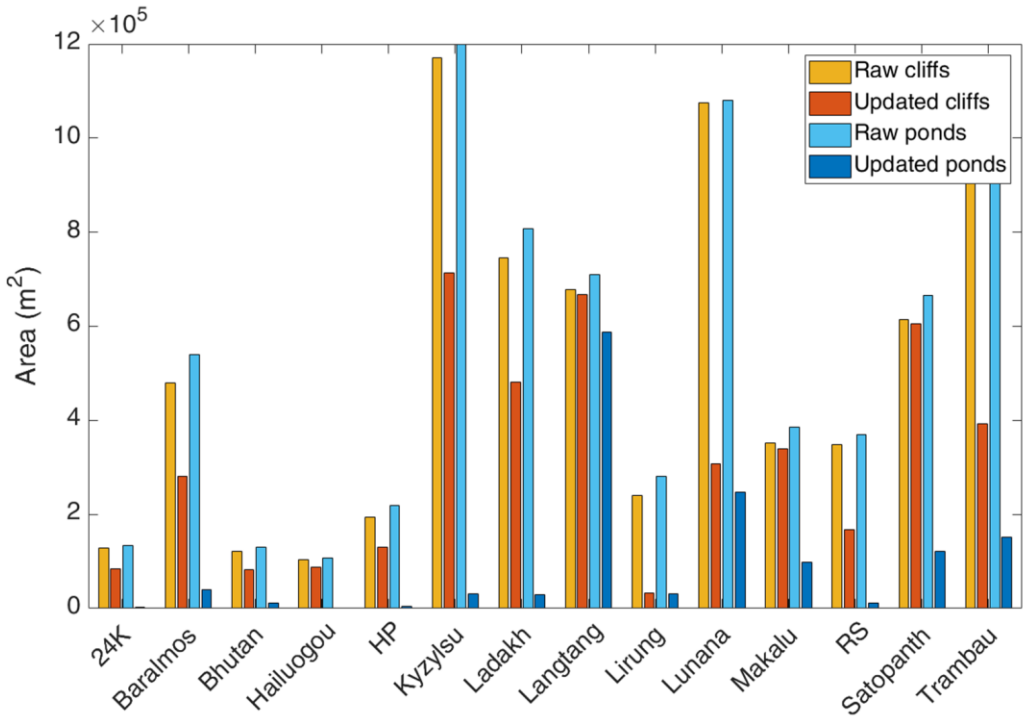

Figure S8: Cliff and pond area before and after manual trimming of automatically derived outlines for each scene.

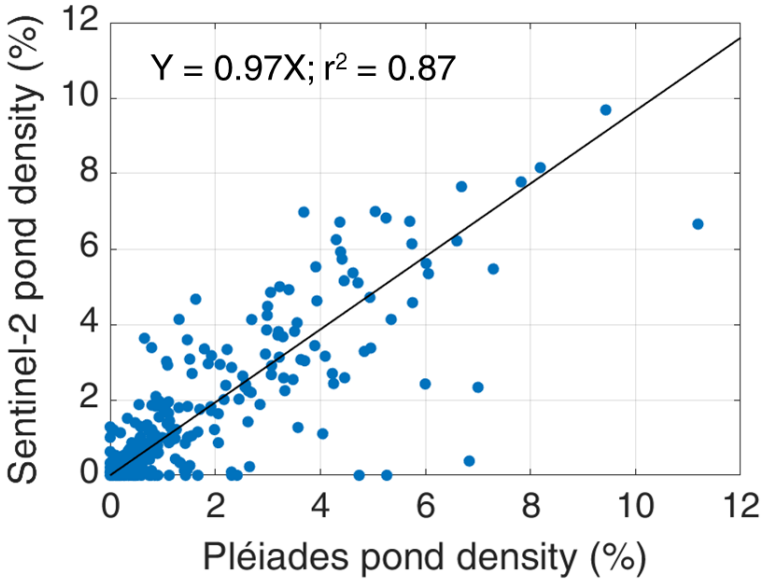

Figure S9: S2 ponds VS Pléiades ponds for each bin.

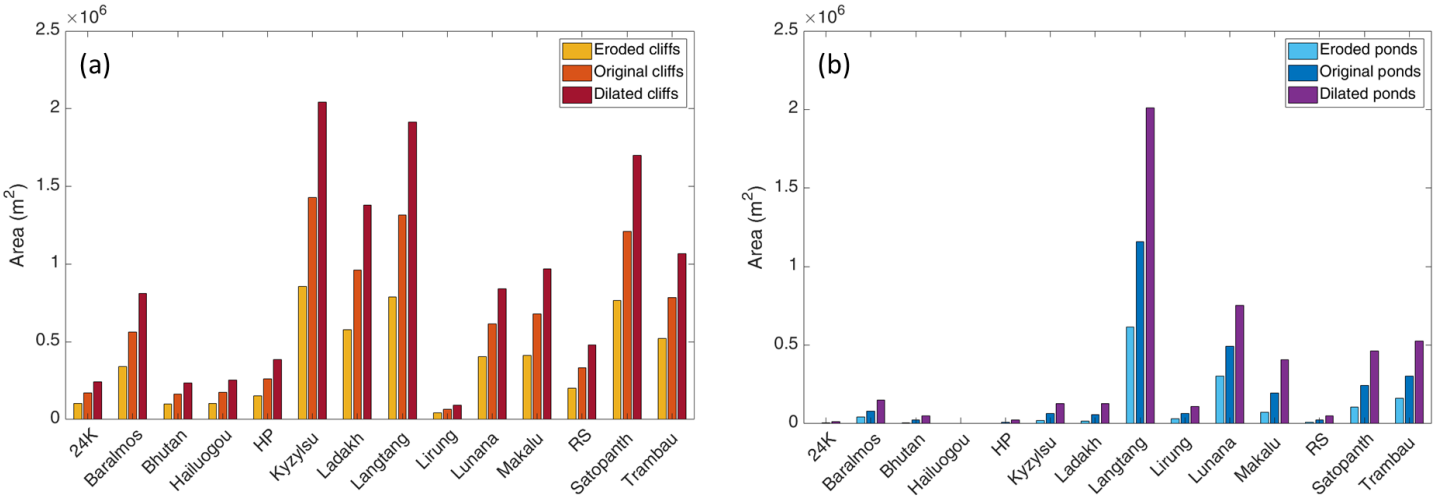

Figure S10: (a) Cliff and (b) pond original, dilated and eroded area for each scene.

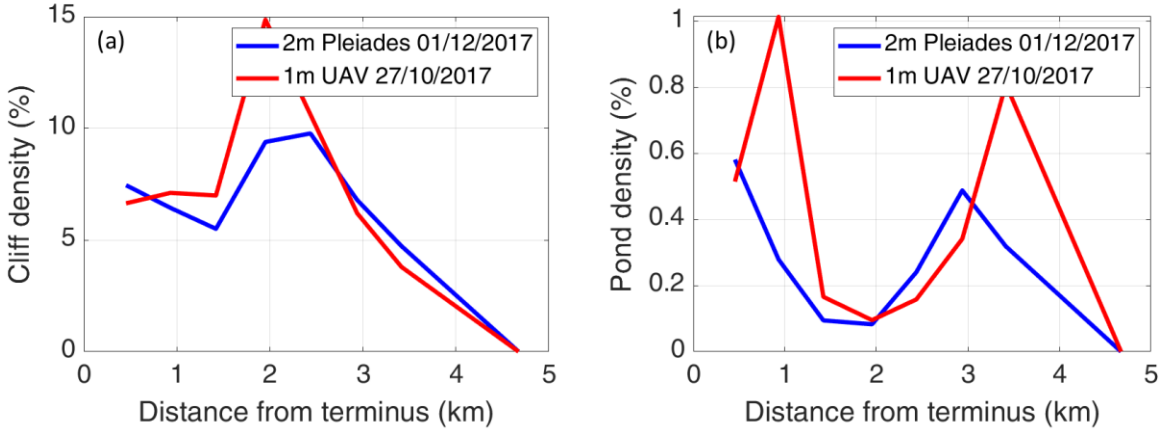

Figure S11: Cliff (a) and pond (b) density on Trakarding Glacier as a function of distance from the terminus calculated based on the Pléiades outlines (01/12/2017) from this study and those independently derived using a 1m UAV orthoimage (27/10/2017).

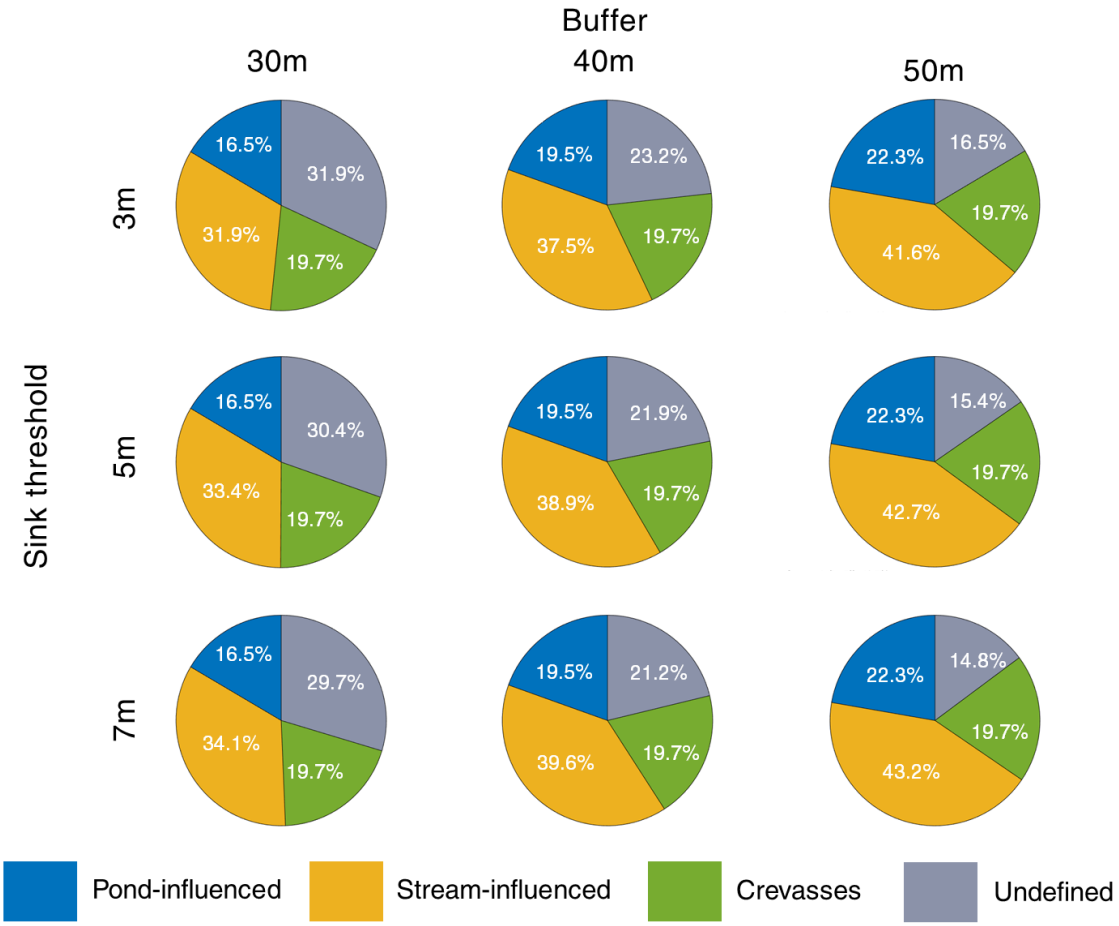

Figure S12: Area proportion of each cliff category depending on the DEM sink filling threshold for the mapping of the streams and the stream and pond buffer, for all cliff pixels.

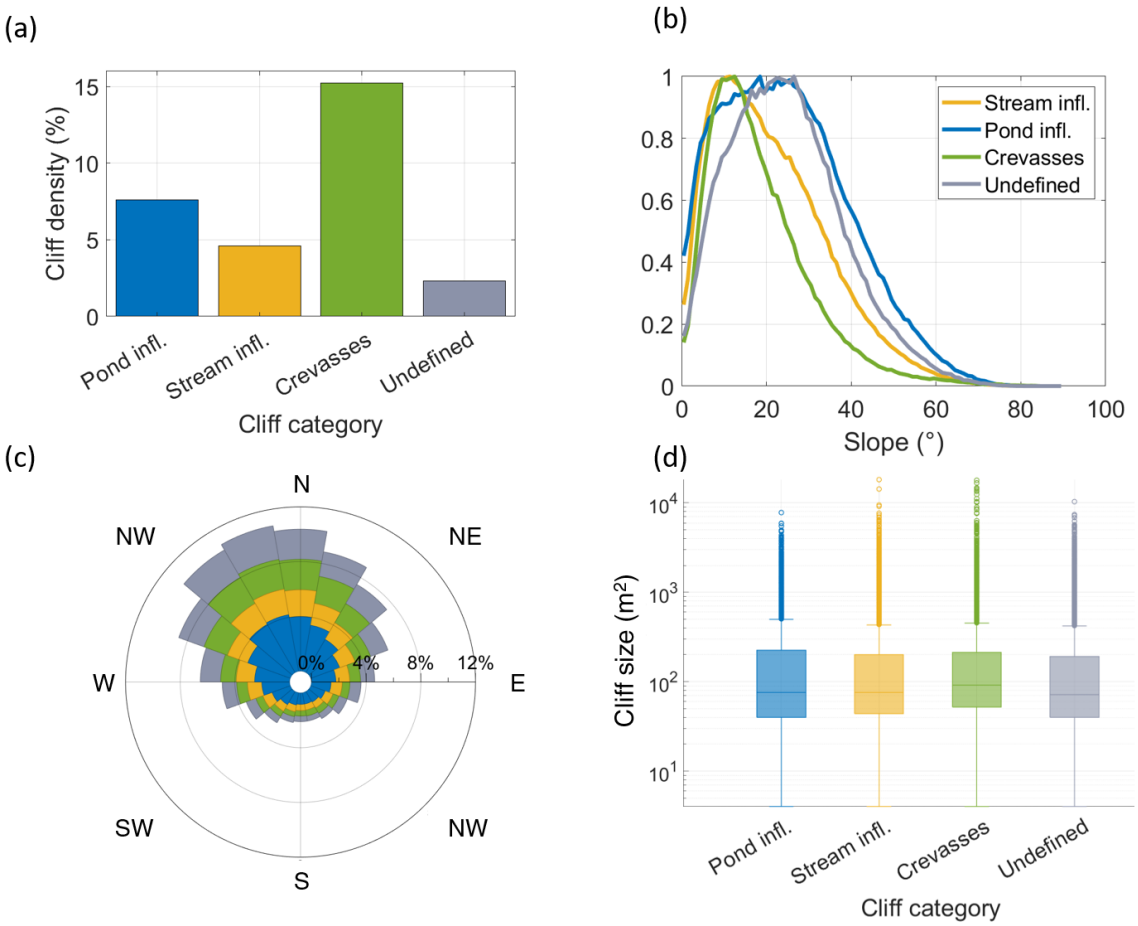

Figure S13: (a) Ice cliff density within buffer areas, (b) normalised slope distribution and (c) aspect distribution for all cliff pixels. (d) Size distribution of individual cliffs (defined as 8-connected objects in the cliff map) showing the median, 25th and 75th percentiles. The circles are considered as outliers.

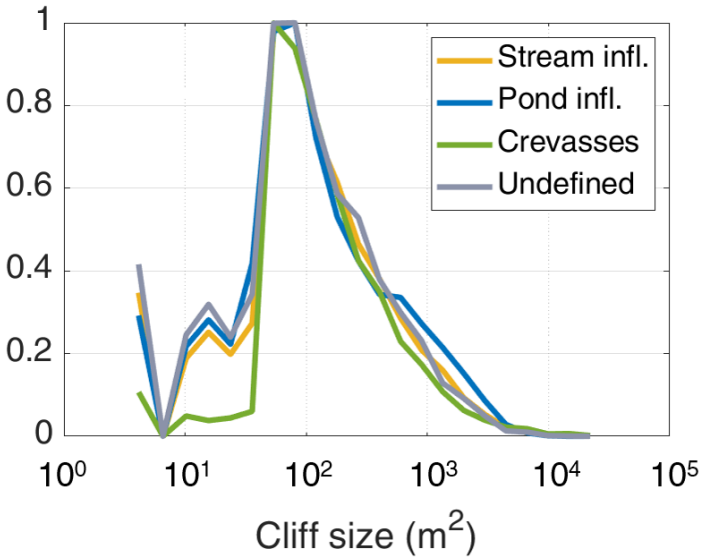

Figure S14: Normalised size distribution of the different cliff categories. The distributions are limited by the resolution of the Pléiades pixels (4 m^2), and the ability of the operator to identify ice cliffs less than ~25 pixels or 100 m^2 (Kneib et al., 2020).

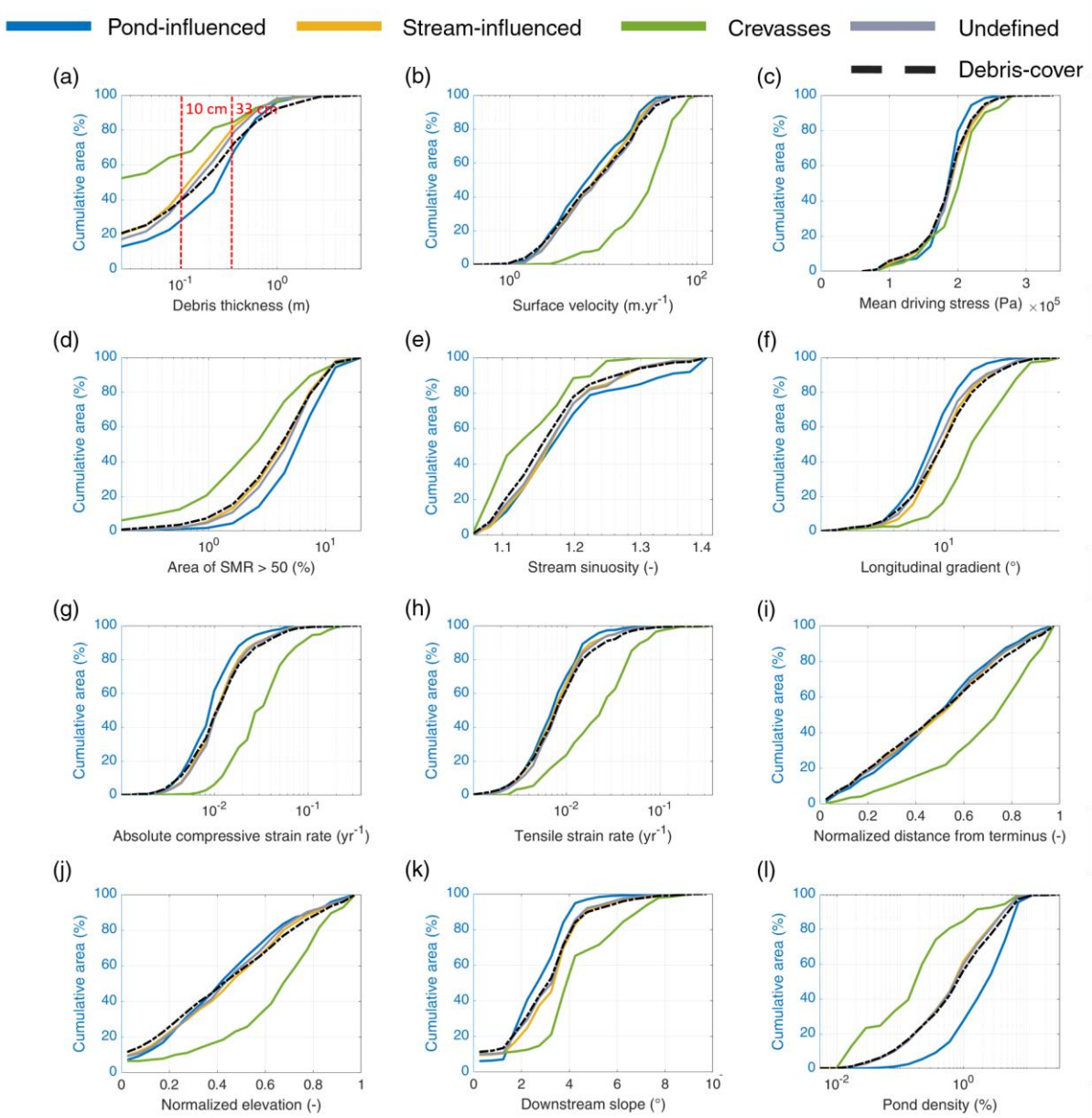

Figure S15: Cliff cumulative area in each category as a function of various metrics for all bins of all glaciers where more than 65% of the debris-covered area could be classified. The black line shows the cumulative area of all the bins.

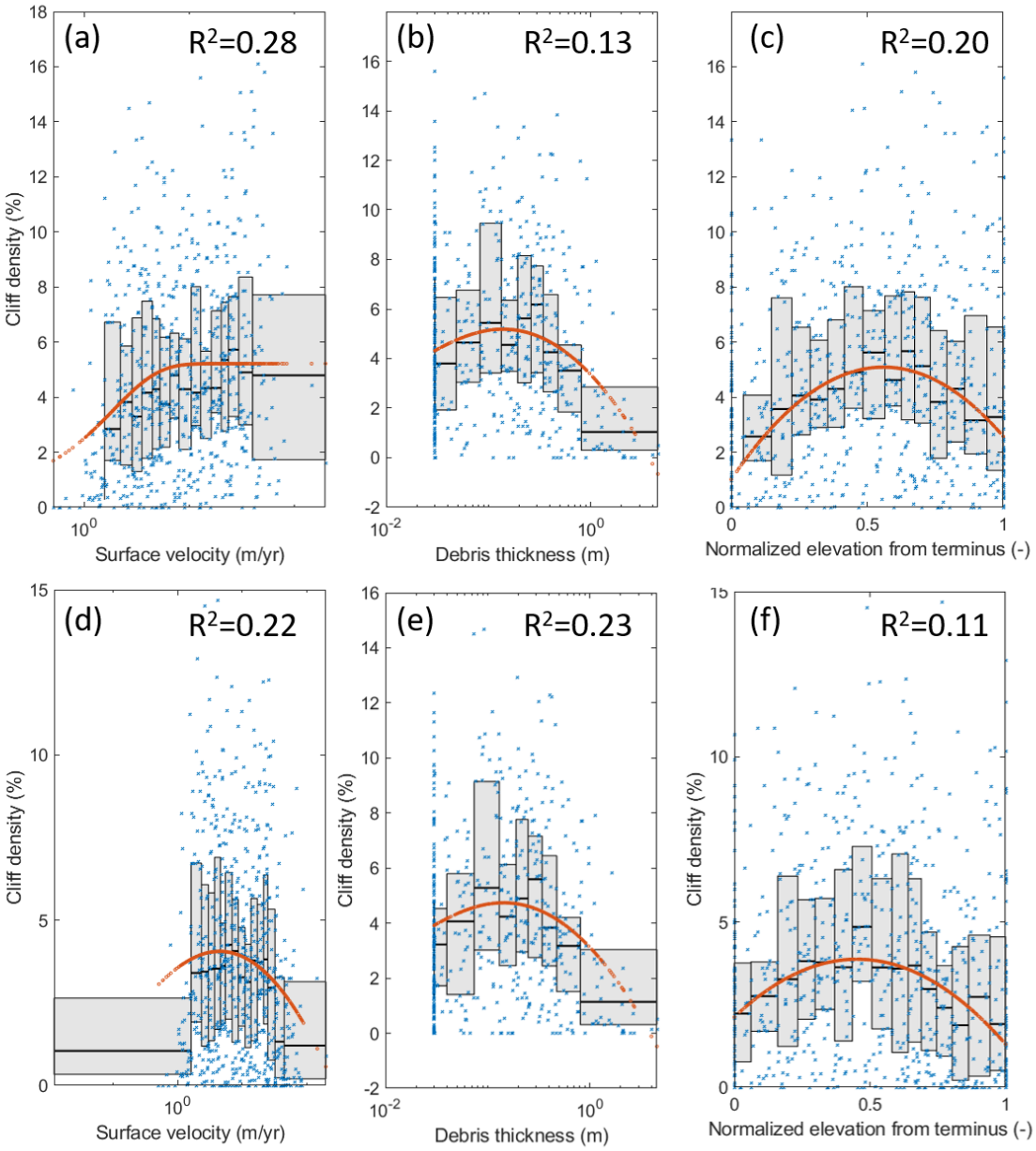

Figure S16: Cliff density with (a-c) and without crevasses (d-f) as a function of (a,d) surface velocity, (b,e) debris thickness and (c,f) normalized elevation from terminus for all bins of all glaciers for which more than 65% of the debris-covered area could be classified. The grey zones indicate the median and the interquartile range where each bin includes one tenth of the data. The red dots show a polynomial fit to the median values and the R^2 the results of this fit for the binned data.

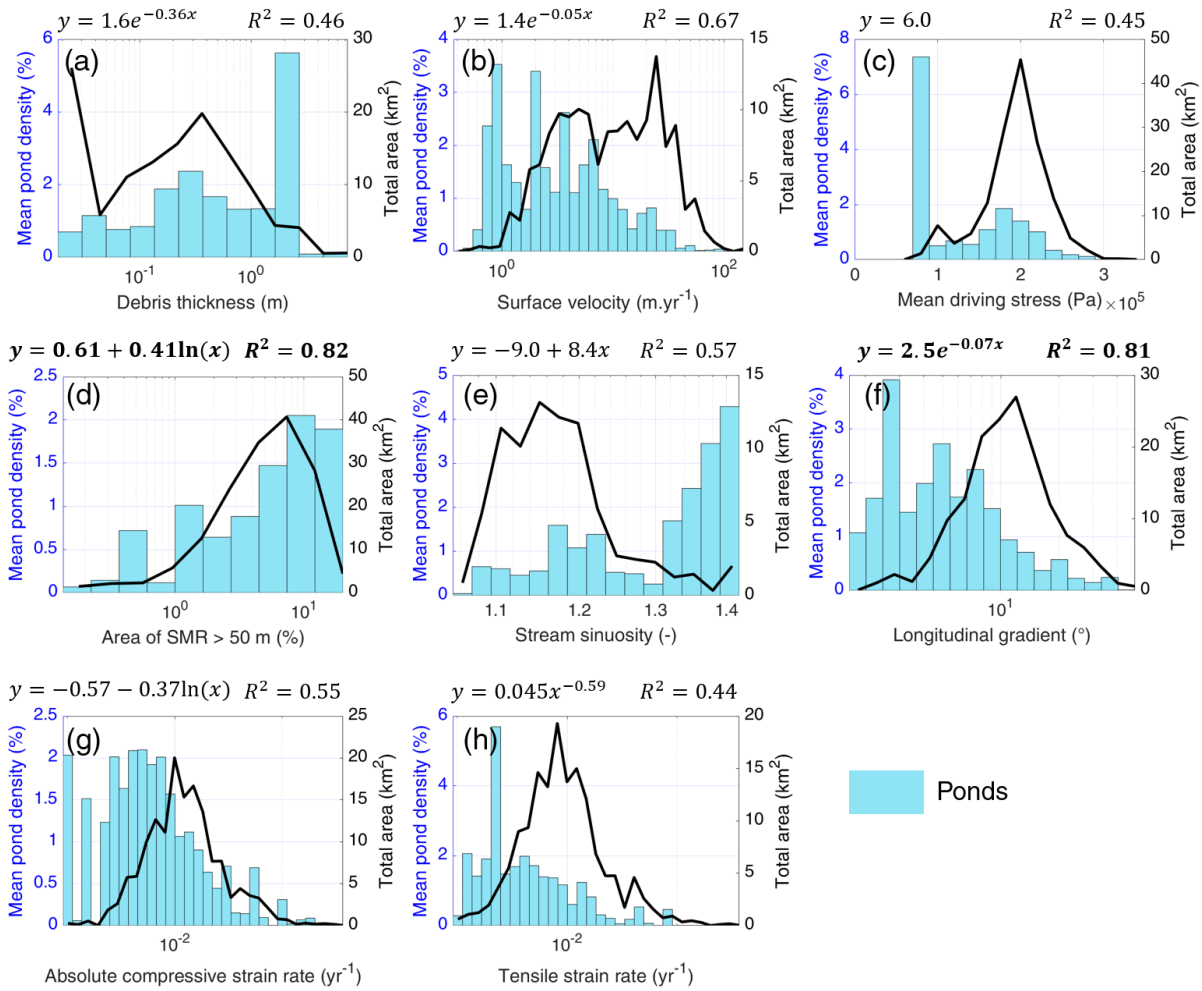

Figure S17: Mean pond density as a function of different variables for all bins of all glaciers where more than 65% of the debris-covered area could be classified: (a) debris thickness, (b) surface velocity, (c) mean driving stress, (d) 'hummockiness', (e) stream sinuosity, (f) longitudinal gradient, (g) absolute compressive strain rate and (h) tensile strain rate. The black line shows the area distribution of all the bins. The equations on top of the plot show the best linear relationships that could be found between the mean pond density (y) and the different variables (x), with their respective R^2 value, only accounting for the points with more than 10 observations. The relationships with an R^2 value higher than 0.8 are indicated in bold.

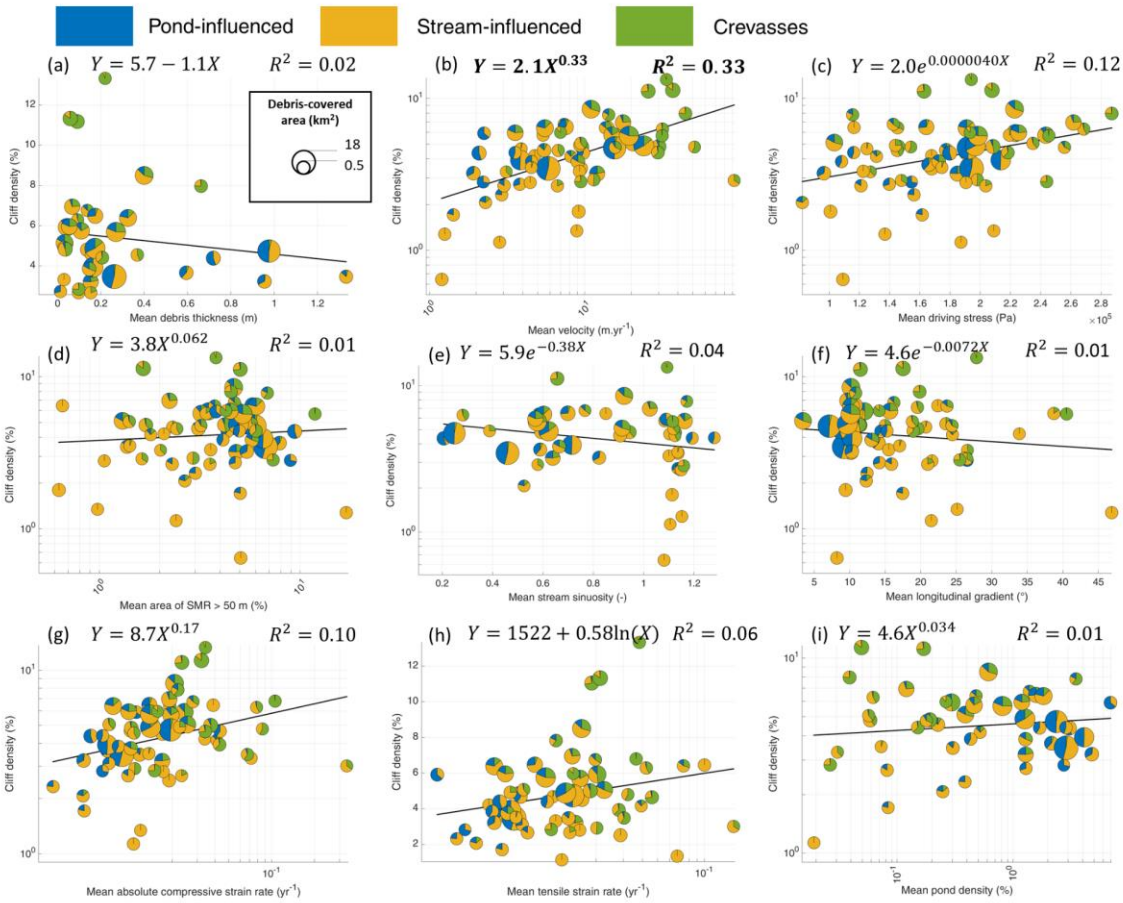

Figure S18: Cliff density for all glaciers where more than 65% of the debris-covered area could be classified, as a function of mean (a) debris thickness, (b) velocity, (c) driving stress, (d) hummockiness, (e) stream sinuosity, (f) longitudinal gradient, (g) compressive strain rate, (h) tensile strain rate, (i) pond density.

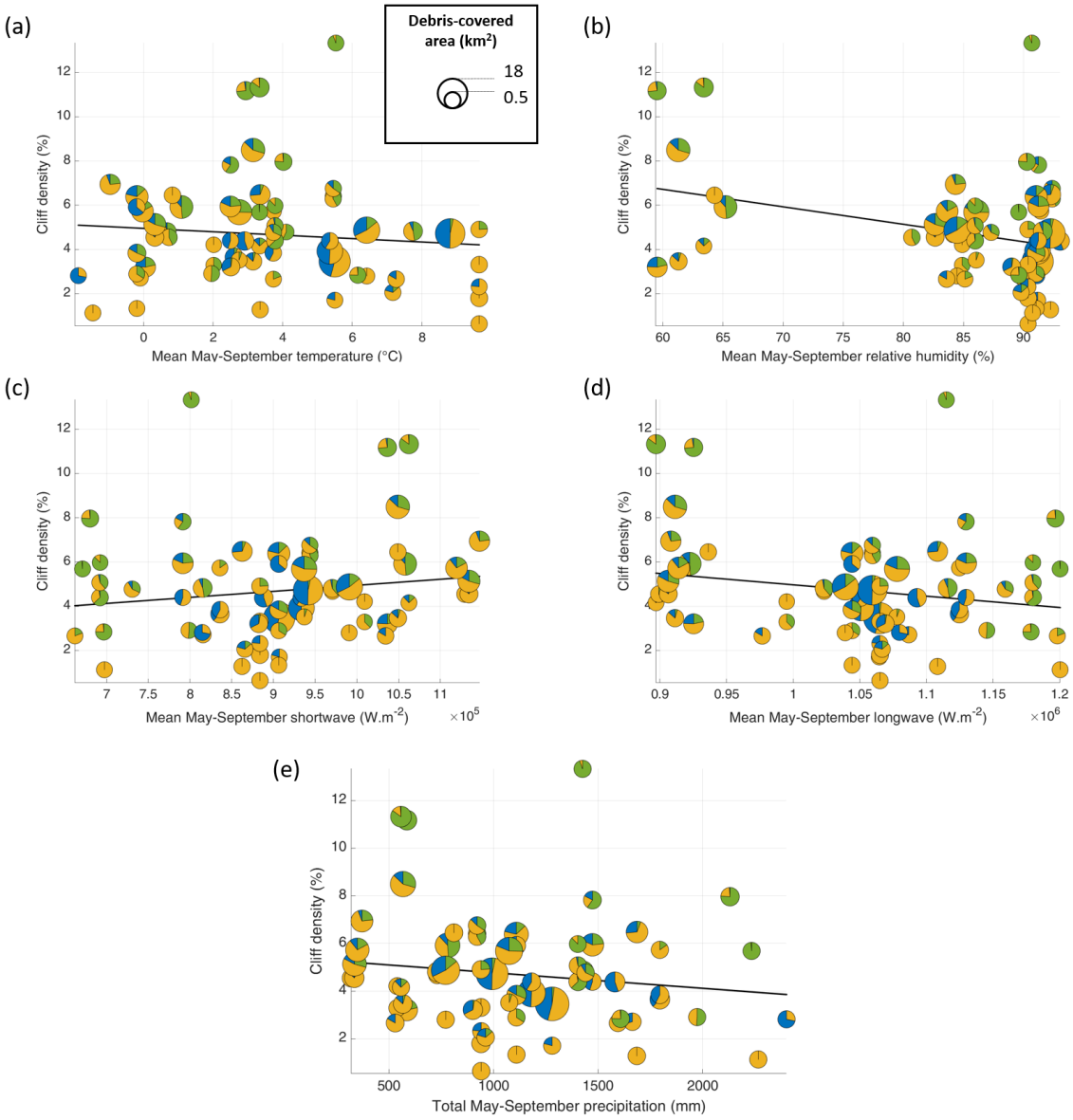

Figure S19: Cliff density for all glaciers where more than 65% of the debris-covered area could be classified, as a function of May-September (a) air temperature, (b) relative humidity, (c) incoming shortwave radiation and (d) incoming longwave radiation. The climatic variables are from ERA5-Land reanalysis data (Muñoz-Sabater et al., 2019), and the air temperature was lapsed to the mean elevation of the debris-covered area considering the mean above-debris lapse rates (-0.0088°C.m^{-1}) following Shaw et al. (2016). The proportion of undefined cliffs was not represented for better readability.

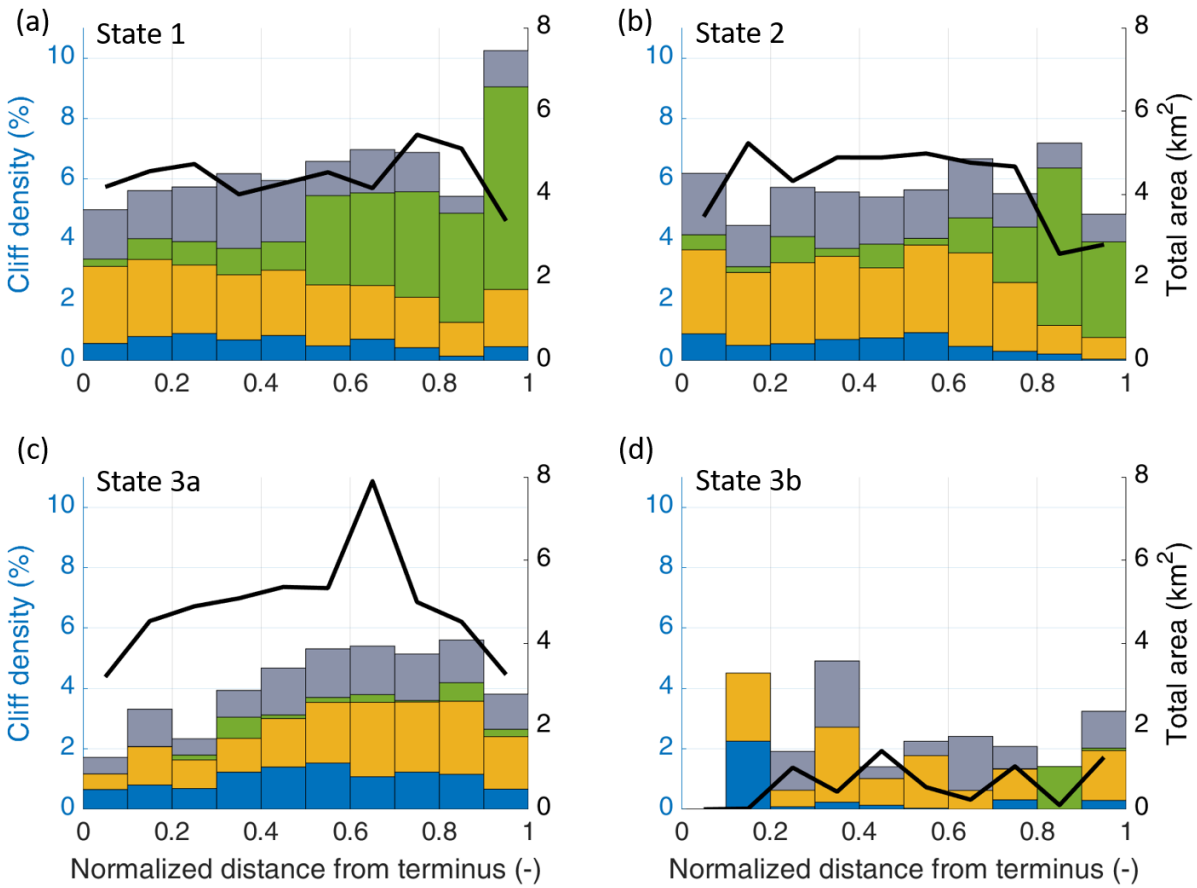

Figure S20: Mean cliff density split by cliff category for all bins of all glaciers where more than 65% of the debris-covered area could be classified as a function of normalized distance from the terminus. The glaciers are split per glacier evolution states (a) 1, (b) 2, (c) 3a and (d) 3b. The categorization is based on the segmentation indicated in blue dashed lines in figure 4.

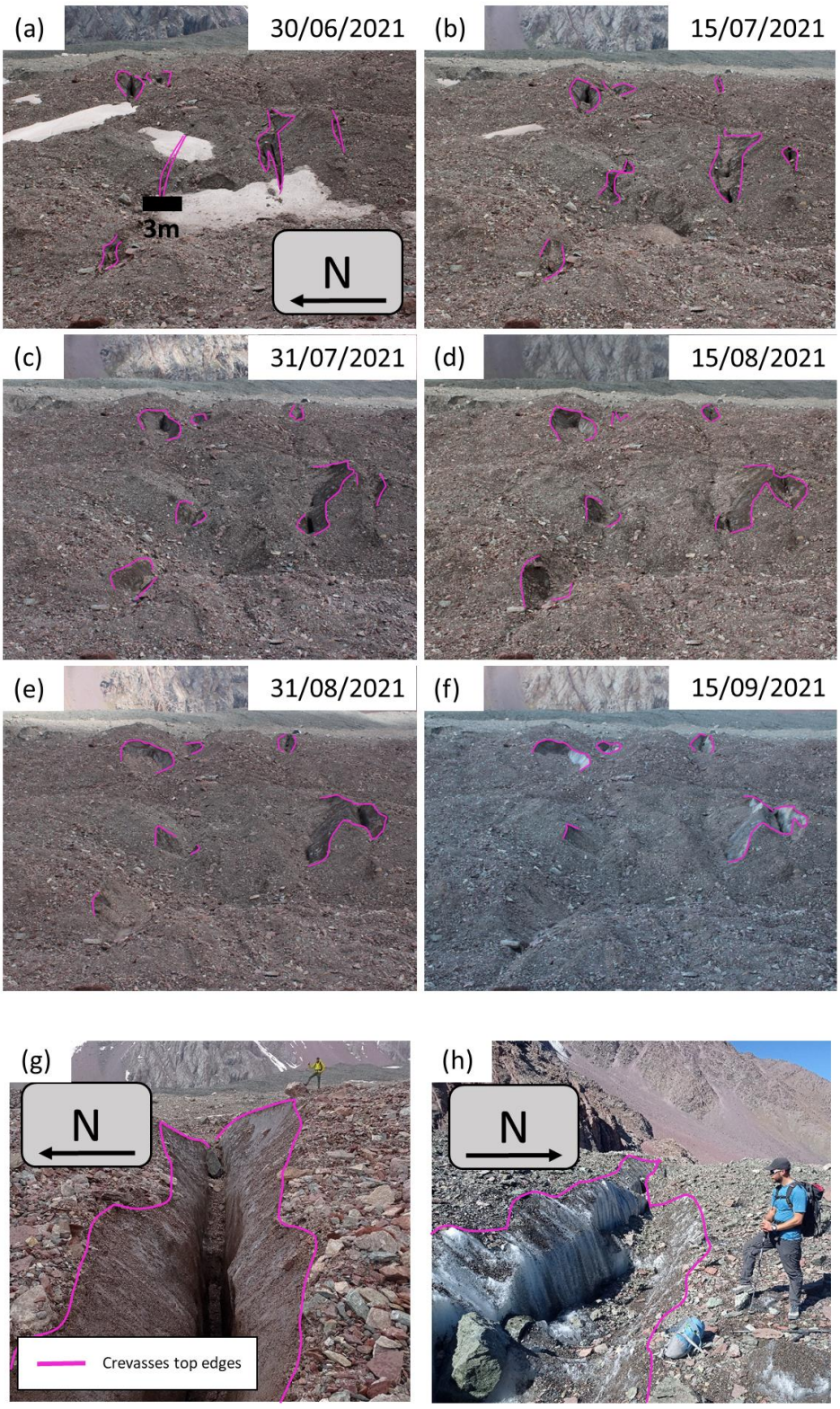

Figure S21: Crevasses on Kyzylsu Glacier (a-f) at bi-weekly time-steps during the 2021 melt season and (g-h) close-up views of other crevasses in September 2021 (image credit: Marin Kneib).

Table S1. Multi-temporal UAV datasets. The Trakarding data are from Sato et al. (2021), the 23K and 24K data are from Chuanxi et al. (in prep) and the Langtang and Lirung data are from Kraaijenbrink et al. (in prep) as well as from Immerzeel et al. (2014) and Brun et al. (2016).

Glacier	UAV survey dates	Original DEM and ortho resolution (m)	Resampled DEM resolution (m)	Survey domain area (km^2)	Survey domain (% total debris-covered area)
Trakarding (RGI-15.03448)	27/10/2017	0.2	1	2.9	43
	18/10/2018	0.2			
	18-19/10/2019	0.2			
23K (RGI-15.11752)	27/09/2018	0.08	1	0.51	38
	13/08/2019	0.07			
	12/10/2019	0.07			
	20/08/2020	0.08			
	22/10/2020	0.1			
24K (RGI-15.11758)	27/09/2018	0.09	1	0.59	64
	13/08/2019	0.07			
	12/10/2019	0.07			
	20/08/2020	0.13			
	22/10/2020	0.09			
Langtang (RGI-15.04121)	07/05/2014	0.1	1	1.5	8.2
	22/10/2015	0.1			
	04/05/2016	0.1			
	09/10/2016	0.1			

	26/04/2017	0.1			
	22/10/2017	0.1			
	22/04/2018	0.1			
Lirung (RGI-15.04045)	18/05/2013	0.1	1	0.47	0.49
	22/10/2013	0.1			
	01/05/2014	0.1			
	10/2014	0.25			
	18/10/2015	0.1			
	30/04/2016	0.1			
	06/10/2016	0.1			
	20/04/2017	0.1			
	19/10/2017	0.1			
	28/04/2018	0.1			

Table S2. Pléiades stereo-images used in this study.

Acquisition name	Acquisition date	Location (coordinates of center point)	Number of debris-covered glaciers in scene (>65% of debris-covered area mapped)	Source
24K	20/09/2021	29.77°N, 95.70°E	5	Royal Society
Baralmos	13/09/2021	39.03°N, 71.37°E	4	ERC RAVEN
Bhutan	08/11/2017	28.10°N, 90.27°E	4	PGO
Hailuogou	29/09/2021	29.56°N, 101.94°E	3	Royal Society
HP	12/09/2020	32.25°N, 77.43°E	5	PGO
Kyzylsu	19/09/2021	39.06°N, 71.50°E	5	ERC RAVEN
Ladakh	24/09/2020	33.76°N, 76.30°E	5	PGO
Langtang	14/06/2019	28.28°N, 85.73°E	8	ERC RAVEN
Lirung	13/10/2019	28.23°N, 85.54°E	3	ERC RAVEN
Lunana	07/11/2017	28.12°N, 90.15°E	1	PGO
Makalu	16/10/2018	27.85°N, 87.04°E	7	PGO
RS	15/10/2017	28.76°N, 83.52°E	8	PGO
Satopanth	18/09/2021	30.78°N, 79.35°E	5	ERC RAVEN
Trambau	01/12/2017	27.89°N, 86.51°E	7	PGO

Table S3. Characteristics of each studied glacier. The mean glacier aspect was obtained from the AW3D 30m DEMs (Tadono et al., 2014).

RGI Region	RGI ID	Pléiades scene	Glacier state	Glacier area (km^2)	Debris-covered area (km^2)	Debris-covered area (%)	Area classified (%)	Mean glacier aspect (°)	Cliff density (%)	Pond density (%)
13	19878	Baralmos	2	30.04	8.33	28	74	-62	5.6	0.1
13	19863	Baralmos		8.57	3.81	44	16	4	6.7	0.1
13	18355	Baralmos		1.39	0.23	17	63	-177	2.9	0
13	19836	Baralmos	2	1.65	0.88	53	81	-75	4.8	0

13	19851	Baralmos	2	7.77	5.01	64	93	-3	2.9	1.0
13	19833	Baralmos		1.69	1	59	88	-56	1.0	0
15	02369	Bhutan		4.92	1.44	29	46	156	6.4	0.6
15	02370	Bhutan	1	1.98	0.26	13	71	-177	4.7	0
15	02372	Bhutan	2	1.74	0.76	44	91	-151	5.4	0.2
15	02373	Bhutan	1	10.71	0.65	6	87	-108	5.9	0.1
15	02375	Bhutan	2	5.1	0.77	15	88	-70	6.4	0.9
14	15547	Himachal Pradesh	3a	2.6	0.55	21	68	-99	4.7	0
14	15491	Himachal Pradesh		5.51	1.72	31	41	-66	2.2	0.1
14	15536	Himachal Pradesh	2	4.48	2.73	61	94	-32	4.7	0.1
14	15988	Himachal Pradesh		15.04	4.04	27	54	-17	2.0	0
14	15471	Himachal Pradesh	3a	0.62	0.17	27	97	-17	3.1	0
14	15990	Himachal Pradesh		14.42	1.96	14	55	-14	1.9	0
14	15989	Himachal Pradesh		9.29	2.08	22	51	135	1.4	0.3
14	15437	Himachal Pradesh	3a	1.03	0.1	10	85	-110	4.1	0
14	15991	Himachal Pradesh		3.37	0.76	23	83	-61	3.7	0
13	19847	Kyzylsu	1	9.77	3.01	31	95	-4	10.9	0.1
13	19824	Kyzylsu	2	3.73	2.07	55	98	-24	3.3	0.2
13	18354	Kyzylsu	2	22.76	9.11	40	91	10	8.0	0.2
13	19807	Kyzylsu	1	12.69	4.06	32	85	-11	11.2	0
13	18358	Kyzylsu	2	0.52	0.34	65	87	29	3.8	0.2
14	18750	Ladakh	1	34.1	5.37	16	75	32	6.7	0.1
14	18904	Ladakh	3a	2.92	1.02	35	72	-18	4.5	0
14	18909	Ladakh	3a	14.58	2.76	19	72	41	4.4	0.1
14	18948	Ladakh	1	69.97	7.55	11	70	26	4.7	0.3
14	18940	Ladakh	2	22.25	6.97	31	89	43	5.4	0.2
15	09457	Langtang		12.32	5.6	45	50	-95	2.6	1.3
15	04119	Langtang	3a	13.65	2.88	21	97	159	3.0	1.8
15	04121	Langtang	3a	54.8	18.23	33	100	-173	3.0	2.2
15	09474	Langtang	3a	24.79	11.69	47	88	160	3.3	3.4
15	09476	Langtang	2	3.73	1.19	32	108	-161	1.9	7.2
15	04036	Langtang	3b	1.3	0.65	50	74	116	1.7	0.1
15	09475	Langtang	3a	4.35	3.41	78	94	80	3.5	2.5
15	04176	Langtang	2	19.9	5.08	26	106	-81	5.9	1.3
15	04308	Langtang	3b	1.22	0.73	60	108	-74	1.0	0.1

15	03957	Lirung	2	0.68	0.48	71	76	-175	2.9	0
15	04045	Lirung	3a	6.33	0.96	15	92	156	3.4	0.3
15	03956	Lirung	3a	1.45	0.7	48	79	-156	1.3	0
15	09457	Lirung		12.32	5.6	45	36	-95	1.0	0.9
15	02358	Lunana	2	11.23	7.16	64	37	136	0.8	4.0
15	02229	Lunana		32.47	15.96	49	93	179	4.0	1.3
15	03401	Makalu	2	7.28	2.81	39	80	-124	3.6	0.8
15	03378	Makalu	3b	2.81	0.74	26	78	-110	2.2	1.2
15	03366	Makalu		26.5	3.01	11	49	124	6.9	0.3
15	03849	Makalu	3a	0.55	0.28	51	96	171	2.3	1.9
15	03372	Makalu	1	1.44	0.51	35	73	67	2.7	0
15	03727	Makalu	3b	0.92	0.45	49	76	15	4.3	0
15	03619	Makalu	3a	30.73	7.9	26	90	119	5.8	1.1
15	03728	Makalu	3a	9.88	1.45	15	80	-120	3.9	1.2
15	04870	Rikha Samba	2	4.77	1.05	22	70	-59	4.8	0
15	04591	Rikha Samba	3b	3.04	1.07	35	74	168	0.7	0.4
15	04843	Rikha Samba	3b	6.69	1.73	26	82	93	2.1	0.1
15	04411	Rikha Samba	3b	1.77	0.65	37	88	139	2.1	0.3
15	04410	Rikha Samba	3b	1.59	0.76	48	95	10	1.9	0.2
15	04854	Rikha Samba	2	4.88	0.78	16	88	-126	4.9	0.1
15	04830	Rikha Samba	1	30.93	3.49	11	90	-95	4.7	0.4
15	04568	Rikha Samba	1	6.33	0.66	10	71	79	12.8	0
15	07122	Satopanth	1	34.86	12.42	36	91	97	4.3	0.7
15	07190	Satopanth	3b	1.22	0.37	30	83	180	2.8	0
15	06942	Satopanth	3a	1.7	0.46	27	89	-4	3.6	0.1
15	07123	Satopanth		19.27	4.77	25	64	42	6.3	0.2
15	06861	Satopanth	3b	3.29	1.07	33	68	35	2.5	0.1
15	07122	Satopanth	1	22.95	10.95	48	89	57	5.1	0.4
15	03776	Trambau		0.41	0.18	44	83	-112	2.1	0.3
15	03782	Trambau	3b	1.73	0.59	34	93	170	1.1	0
15	03531	Trambau		1.41	1.06	75	52	-111	3.2	0.6
15	03498	Trambau		3.31	1.18	36	38	-139	3.2	0
15	03448	Trambau		30.97	6.69	22	57	-99	6.0	0.7
15	03943	Trambau	1	1.99	0.81	41	76	-166	7.1	2.6
15	03926	Trambau	3a	1.19	0.86	72	89	169	3.3	2.1
15	03428	Trambau	3a	15.97	6.09	38	68	-136	5.5	0.7

15	03435	Trambau	3a	4.7	2.73	58	95	77	2.9063	3.4
15	09771	Trambau		19.74	5.13	26	39	-143	7.0	0.1
15	09764	Trambau		1.62	0.53	33	81	149	2.0	1.0
15	11750	24K	3b	3.14	0.67	21	100	-3	2.7	0
15	11752	24K	1	4.07	1.34	33	100	85	4.2	0.1
15	11758	24K	2	1.97	0.92	47	100	-66	4.9	0.1
15	11765	24K	2	1.31	0.69	53	100	47	4.6	0.1
15	11760	24K	3a	1.33	0.3	23	100	-11	5.8	0.4
15	07886	Hailuogou	1	19.07	1.57	8	100	93	7.8	0
15	07889	Hailuogou	2	5.44	0.92	17	100	69	2.8	0
15	07894	Hailuogou	1	1.25	0.65	52	100	70	4.4	0

Table S4: Mean and standard deviation of the lognormal distribution of cliff size for the different cliff categories.

Cliff category	Mean	Standard deviation
All	4.46	1.39
Pond-influenced	4.50	1.46
Stream-influenced	4.44	1.41
Crevasses	4.72	1.18
Undefined	4.34	1.42

Table S5: Best fitting relationships between binned density of different cliff categories (As shown in Fig. 4) and different predictors. Highlighted in green, blue and yellow are respectively the best, second best and third best relationships (based on R^2).

Cliff type	Velocity	Debris thickness	Longitudinal gradient	Driving stress	Pond density
All	R^2=0.73 $Y = 3.7+0.10X$	R^2=0.94 $Y = 6.0e^{-0.48X}$	R^2 =0.17 $Y = 3.2+0.73\ln(X)$	R^2=0.58 $Y = 2.9+(1.3x10^{-5})X$	R^2=0.12 $Y =5.0e^{-0.013X}$
Pond-infl.	R^2 =0.34 $Y = 0.94e^{-0.019X}$	R^2 =0.27 $Y = 0.95e^{-0.28X}$	R^2=0.88 $Y = 1.8e^{-0.084X}$	R^2=0.15 $Y = 1.1e^{-0.0000036X}$	R^2=0.95 $Y = 0.74X^{0.59}$
Stream-infl.	R^2=0.08 $Y = 2.0-0.0099X$	R^2=0.86 $Y = 2.5e^{-0.48X}$	R^2=0.03 $Y = 1.8-0.0078X$	R^2=0.07 $Y=1.7+(2.0x10^{-6})X$	R^2=0.74 $Y = 2.2e^{-0.053X}$
Crevasses	R^2=0.83 $Y = -0.65+0.12X$	R^2=0.24 $Y = 0.32-0.15\ln(X)$	R^2=0.52 $Y = 0.11X^{0.87}$	R^2=0.36	R^2=0.60 $Y = 0.23X^{-0.51}$

				$Y = -1.0+(1.3x10^{-5})X$	
Undefined	$R^2=0.14$ $Y = 0.94X^{0.14}$	$R^2=0.74$ $Y = 1.9e^{-0.57X}$	$R^2=0.21$ $Y = 1.5e^{-0.012X}$	$R^2=0.01$ $Y = 1.4+(3.0x10^{-7})X$	$R^2=0.58$ $Y = 1.6e^{-0.052X}$

Cliff type	Absolute compressive strain rate	Tensile strain rate	Hummockiness	Stream sinuosity	Normalized distance from terminus
All	$R^2=0.82$ $Y = 11+1.3\ln(X)$	$R^2=0.55$ $Y = 11X^{0.15}$	$R^2=0.60$ $Y = 5.0X^{0.038}$	$R^2=0.08$ $Y = 3.1e^{0.44X}$	$R^2=0.77$ $Y = 4.1e^{0.51X}$
Pond-infl.	$R^2=0.62$ $Y = 1.0e^{-20X}$	$R^2=0.82$ $Y = 1.1e^{-34X}$	$R^2=0.93$ $Y = 0.26+0.076X$	$R^2=0.22$ $Y = 0.42X^{2.5}$	$R^2=0.09$ $Y = 0.85+0.065\ln(X)$
Stream-infl.	$R^2=0.03$ $Y = 2.1X^{0.04}$	$R^2=0.74$ $Y = 2.4e^{-16X}$	$R^2=0.22$ $Y = 1.5X^{0.083}$	$R^2=0.23$ $Y = 1.4+4.9\ln(X)$	$R^2=0.02$ $Y = 2.0e^{-0.065X}$
Crevasses	$R^2=0.88$ $Y = 403X^{1.6}$	$R^2=0.84$ $Y = -0.17+103X$	$R^2=0.72$ $Y = 1.8-0.44\ln(X)$	$R^2=0.12$ $Y = 2.1X^{-6.8}$	$R^2=0.84$ $Y = 0.18e^{2.9X}$
Undefined	$R^2=0.14$ $Y = 1.9X^{0.092}$	$R^2=0.42$ $Y = 1.6e^{-8.7X}$	$R^2=0.54$ $Y = 1.0X^{0.15}$	$R^2=0.01$ $Y = 2.2e^{-0.39X}$	$R^2=0.02$ $Y = 1.4e^{-0.075X}$

Cliff type	Normalized elevation	Downstream slope
All	$R^2=0.59$ $Y = 6.0X^{0.17}$	$R^2=0.64$ $Y = 4.1e^{0.077X}$
Pond-infl.	$R^2=0.09$ $Y = 0.92e^{-0.36X}$	$R^2=0.51$ $Y = 1.3-0.17X$
Stream-infl.	$R^2=0.05$ $Y = 2.0+0.087\ln(X)$	$R^2=0.05$ $Y = 2.10e^{-0.030X}$
Crevasses	$R^2=0.72$ $Y = 0.18e^{2.8X}$	$R^2=0.69$ $Y = -1.1+0.68X$
Undefined	$R^2=0.02$ $Y = 1.4e^{-0.13X}$	$R^2=0.15$ $Y = 1.6e^{-0.041X}$